Research Article

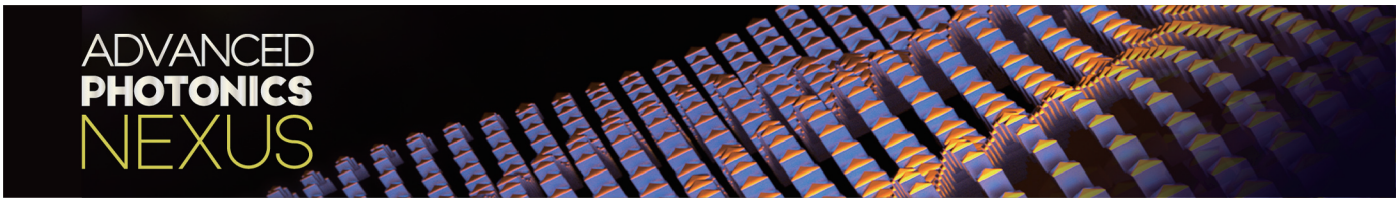

Dissipative soliton breathing dynamics driven by desynchronization of orthogonal polarization states

Zhiwei Huang,[a] Sergey Sergyev,[b,*] Qing Wang,[b] Hani Kbashi,[b] Dmitrii Stoliarov,[b] Qianqian Huang,[a] Yuze Dai,[c] Zhijun Yan,[c] and Chengbo Mou[a,*]

[a]Shanghai University, Shanghai Institute for Advanced Communication and Data Science, Key Laboratory of Specialty Fiber Optics and Optical Access Networks, Joint International Research Laboratory of Specialty Fiber Optics and Advanced Communications, Shanghai, China
[b]Aston University, Aston Institute of Photonic Technologies, Birmingham, United Kingdom
[c]Huazhong University of Science and Technology, School of Optical and Electronic Information and NGIA, Wuhan, China

Abstract. Breathing solitons, i.e., dynamic dissipative solitons with oscillating pulse shape and energy caused by different mechanisms of spatiotemporal instabilities, have received considerable interest from the aspects of nonlinear science and potential applications. However, by far, the study of breathing solitons is still limited within the time scale of hundreds of cavity round trips, which ignores the slow dynamics. To fill this lacuna, we theoretically investigate a new type of vector dissipative soliton breathing regime and experimentally demonstrate this concept using mode-locked fiber lasers, which arise from the desynchronization of orthogonal states of polarization (SOPs) in the form of complex oscillations of the phase difference between the states. The dynamic evolution of polarization states of the vector breathings solitons takes the form of a trajectory connecting two quasi-equilibrium orthogonal SOPs on the surface of the Poincaré sphere. The dwelling time near each state is on the scale of a tenth of a thousand cavity round trip times that equals the breathing period, which is up to 2 orders of magnitude longer than that for common breathers. The obtained results can reveal concepts in nonlinear science and may unlock approaches to the flexible manipulation of laser waveforms toward various applications in spectroscopy and metrology.

Keywords: dissipative solitons; polarization dynamics; vector soliton; breather; *Q*-switched mode locking; nonlinear polarization rotation; coupled oscillators.

Received Aug. 13, 2023; revised manuscript received Oct. 7, 2023; accepted for publication Oct. 18, 2023; published online Nov. 23, 2023.

[DOI: 10.1117/1.APN.2.6.066007]

1 Introduction

During the last three decades, the study of flocking birds, supramolecular complexes, neurons in the cortex, modes synchronization in lasers, telecom, and sensing networks mainly focused on revealing the interactions between individual system components that produce large-scale collective patterns.[1–4] However, in the practical context, targeting the collective patterns under demand is challenging due to the limited ability to conduct experiments on manipulating engineering and biological networks' structure.[1–4] The short pulse duration of hundreds of femtoseconds and repetition rates of tens of hundreds of megahertz make mode-locked lasers (MLLs) suitable testbeds for studying the synchronization-driven self-organization in the form of dissipative solitons (DSs)—ubiquitous localized wave packets arising from the balance between dissipative and dispersive effects.[5–27] For example, recently demonstrated orthogonal states of polarization (SOPs) of DSs show a resemblance of coupled oscillators with various synchronization behaviors.[15,28–30] The synchronization through short-range (covalent) and long-range (non-covalent) interactions among DSs toward swarming pulses into different soliton supramolecules hence offers an unprecedented approach to manipulating the collective patterns under controllable laboratory conditions and a short time scale of seconds.[22,23]

*Address all correspondence to Chengbo Mou, mouc1@shu.edu.cn; Sergey Sergyev, s.sergeyev@aston.ac.uk

Short-range interaction through the overlapping of solitons tails results in bound states (BSs) solitons which, in analogy to biochemical and biological supramolecules, are formed by strong covalent bonds, are frequently referred to as soliton molecules, soliton macromolecules, or soliton crystals.[5,20,21] The strong, short-range interactions lead to the narrow spacing of the few pulse widths and locked phase differences between adjacent solitons, resulting in the highly challenging real-time characterization of their detailed temporal structure.[5,20,21] Long-range interactions can be driven by Casimir-like,[19,25] optoacoustic[17,18,20,24] polarization instabilities,[13–16] and soliton-dispersive wave interaction,[6–12,31] leading to the formation of the soliton structures in the form of multi-pulsing, harmonic mode locking, soliton rain, rogue waves, and breathers.[6–20,24,25,31]

Breathing solitons, known as dynamic DSs, typically feature profile and energy oscillation (breath) of DSs with periods from 5 to 100 round trips (RTs).[6–10] Given the strong connection with the Fermi–Pasta–Ulam recurrence,[32,33] i.e., phenomena describing the periodic return of nonlinearly coupled oscillators to their original states, breather solitons, in addition to rogue waves emergence, turbulence, and modulation instability phenomena, have attracted considerable attention in nonlinear optics.[6–10,32,33] Also, the breathing solitons are attractive because of their potential for metrology applications by enabling multiscale dual-comb sources for increased measurement resolution.[34] It was recently found that the breathing soliton emergence in anomalous dispersion MLLs can be driven by modulation instability[10] and a simultaneous effect of the soliton bunching and polarization instability.[14] On the other hand, the breathers in the normal dispersion regime can arise because of Hopf bifurcation[9] and subharmonic entrainment with an integer ratio of the breathing period to the round-trip time.[7]

A recently developed dispersive Fourier transform technique explores conventional soliton breathing regimes, revealing a range of dynamic vector waveforms with the periods of oscillations from tens to hundreds of round trips under the paradigm of coupled Ginzburg–Landau equations.[34–36] However, given the limitations of the theoretical and experimental study in the context of the dynamic range of tens of thousands of RTs, the slow evolution of the breathing waveforms up to hundreds of thousands of RTs is still absent.[34–36]

To fill this lacuna, for the first time, we believe that we have demonstrated a new type of slow soliton breathing dynamics, showing double temporal scale behavior, caused by a vector mechanism allowing the transition from the zero-lag synchronization to phase difference entrainment and finally desynchronization of orthogonal SOPs. We modeled nonlinear polarization rotation (NPR) mode-locked Er fiber laser in the paradigm of coupled oscillators synchronization. Based on the vector model of MLL dynamics, we reveal that the phase desynchronization is connected to the emergence of the so-called spiral chaos in a heteroclinic system,[37,38] from which the trajectory is periodically evolving nearby each of the orthogonal SOPs and is switching between SOPs.[15,28–30] Through Shil'nikov theorem analysis, which defines the conditions of the spiral chaos emergence,[39] we found that the range of the laser parameters for DS breathing dynamics corresponded well to the experimental observation. In stark contrast to slow breathing regimes,[7,9,10,34–36] the observed vector DS breathing dynamics has much more extended periods up to 10,000 RTs and variable pulse shapes with a featured dual-wavelength optical spectrum. The unveiled dependence of the unprecedented long breathing period and shape on the laser parameters can open an avenue to developing new vector approaches of laser dynamics toward various applications in spectroscopy, micromachining, and metrology.

2 Results

2.1 Experimental Results on Vector Breathing Regimes

The MLL we used to conduct the experiment operated under a normal dispersion regime in the telecommunication C-band. Such a type of laser allows the generation of high-energy pulses on which most practical applications rely. The schematic configuration of the laser is shown in Fig. 1(a) (details are in Appendix A). Dispersion engineering is accomplished through a piece of erbium-doped fiber (EDF) with highly positive group velocity dispersion (GVD). The mode-locking mechanism is NPR, where the intrinsic birefringence of optical fiber is used to generate pulse intensity bias through the combination of a fiber polarizer and two polarization controllers (PCs). The NPR mechanism especially benefits routes to vector pulse shaping in the context of the SOPs. The vector features of DS are analyzed through a polarimeter and present dynamic SOP evolution on the surface of the Poincaré sphere in terms of normalized Stokes parameters, total power, degree of polarization (DOP), phase difference, and power for the orthogonal x-/y-polarization components.

Such orthogonal linear polarized fields of DS with correlated phase relation can be treated as a general phase-coupled oscillator, as shown in Fig. 1(b).[34,37,40,41] The slow temporal behavior of coupled oscillators strongly depends on syn-/desyn-chronization of orthogonal fields through a phase change. Therefore, the DS oscillation can be well explained by the general Adler equation,[42] describing the evolution of the phase difference $\Delta\varphi$ between two coupled oscillators.[15,29,42] The Adler equation is represented as

$$\frac{d\Delta\varphi}{dt} = \Delta\Omega - K \cdot \sin(\Delta\varphi), \tag{1}$$

where $\Delta\Omega$ is the frequency difference, and K is the coupling coefficient. In our DS laser, frequency difference depends on the linear and circular birefringence, and the coupling coefficient is a function of the output powers of the orthogonal SOPs, which depends on both the power and ellipticity of the pump light.[15,29] Given the polarization instability, the SOPs' output powers can evolve, which resembles a coupled oscillator with a dynamic coupling regime.[15,29] As follows from the Adler equation, the synchronization ($d\Delta\phi/dt = 0$) exists when $|\Delta\Omega| < |K|$, i.e., continuous-wave mode locking emerges, as shown in Fig. 1(c). On the other hand, when $|\Delta\Omega| > |K|$ holds, chaotic phase difference slips appear that correspond to the breathing dynamics [$\Delta\varphi$ oscillates within a limited range in Fig. 1(d)] and phase entrainment [phase difference oscillations in Fig. 1(e)]. Furthermore, $|\Delta\Omega| < |K|$ indicates a strong coupling regime, while $|\Delta\Omega| > |K|$ represents a decreased or weak coupling regime. Those dynamic phase phenomena have been theoretically confirmed previously in a self-pulsing laser.[15,28,29]

To obtain the slow vector breathing, we first operate the laser under the standard stable DS regime. In contrast to the laser with the scalar breathing dynamics, the reduction of pump power in our laser leads only to the elimination of stable pulses. Alternatively, we obtained a DS breathing by elevating the pump power under a stable DS mode-locking scenario followed

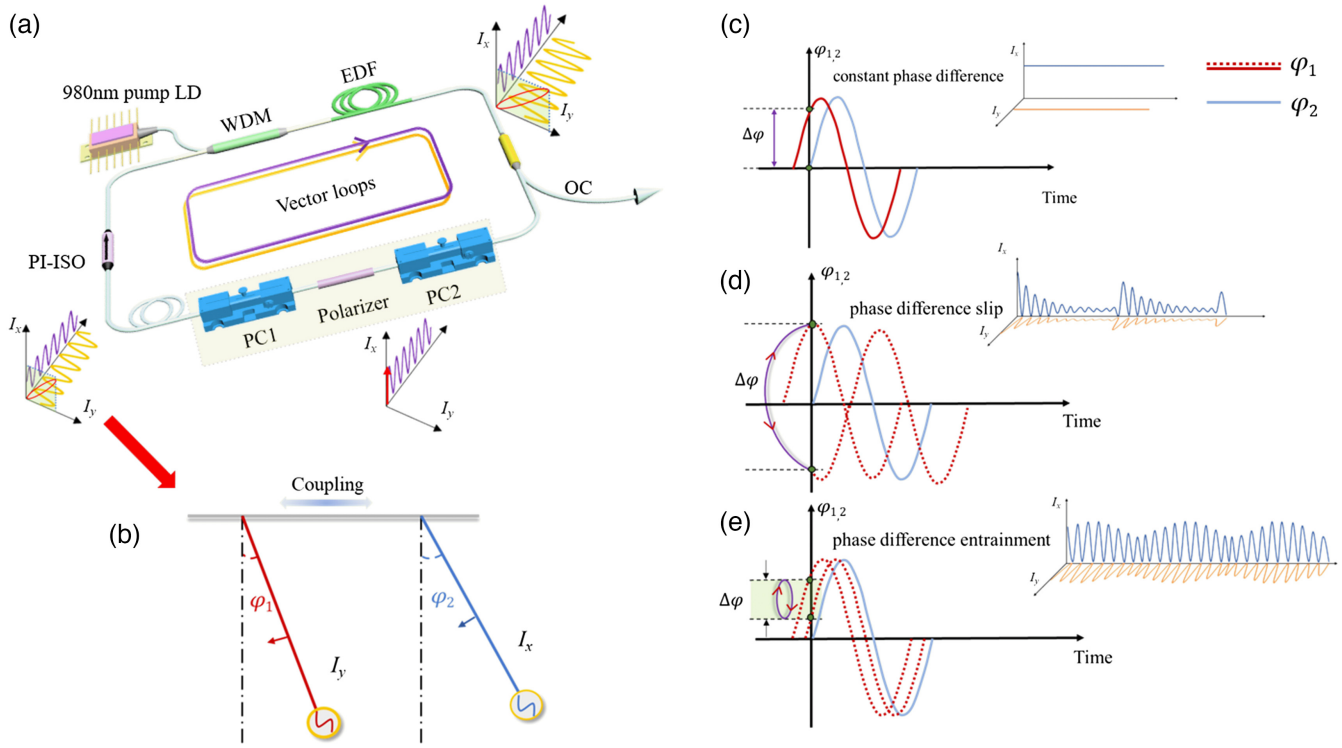

Fig. 1 Vector breathing DS generation in a mode-locked fiber laser. (a) Schematic setup of the NPR mode-locked normal dispersion fiber laser. EDF, erbium-doped fiber; LD, laser diode; PC1 and PC2, polarization controllers; PI-ISO, polarization-insensitive isolator; Polarizer, 45 deg-tilted fiber grating based polarizer; WDM, wavelength division multiplexer; OC, 91:9% output coupler. The opaque yellow area represents the NPR mechanism. (b) A general schematic of orthogonal polarization modes resembled coupled oscillator systems. The two pendula are connected with a common beam indicating the coupling mechanism. Each pendulum has an initial phase angle $\varphi_{1,2}$, initial frequency $f_{1,2}$, and intensity $I_{x,y}$. (c)–(e) The temporal behavior of coupled oscillator model for emitting vector breathing/stable DS. (c) The constant phase difference between orthogonal polarization fields, showing $d\Delta\phi/dt = 0$. In this case, the output DS is synchronized and only stable DS will be generated. (d) Phase difference slip between orthogonal polarization modes, showing $d\Delta\phi/dt \neq 0$ with $|\Delta\Omega| > |K|$. In this case, the phase difference quickly jumps within two fixed points in the vertical axis (blue points). (e) Phase difference entrainment between orthogonal polarization fields, showing $d\Delta\phi/dt \neq 0$ with $|\Delta\Omega| > |K|$. In this case, $\Delta\phi$ oscillates within the region defined by two fixed phase points (blue points in the vertical axis), and the synchronization tends to occur but is never reached.

by fine adjustment of the intracavity PC. The slow vector breathing can be accessed within a range of hundreds of milliwatts of pump power. Figure 2 shows the experimentally observed slow DS breathing dynamics for a normal dispersion laser. Figure 2(a) shows the averaged optical spectra of the breather with a dual-peak signature.[8] Using a high-speed oscilloscope, the temporal intensity distribution of a single DS breather is clearly revealed in Fig. 2(b), illustrating a breather width of 200 RTs and a period of 10,000 RTs. Unlike the scalar DS characterization, through polarimetric measurement, both orthogonal polarization modes can be mapped into the temporal domain, as shown in Fig. 2(c). The disparity in oscillation intensity of orthogonal polarization modes manifests the vector feature of the soliton breathing. Focusing on a 250 μs time scale, the damped oscillation-like behavior consolidates the breathing dynamics. The distinction of the pulses bunches' shape [Figs. 2(b) and 2(c)] between single shot and polarimetric measurement is attributed to the 1 μs time resolution of the polarimeter. In particular, polarimetric measurement gave us a unique opportunity to extract information about the phase difference between orthogonal SOPs and DOP of the slow breathing dynamics. Based on Adler's equation, the phase information allows us to view the synchronization of orthogonal fields. In Fig. 2(d), one can clearly see that periodic phase difference slip in π is related to the breathers' power spike emergence and disappearance. The fast phase difference slip hence results in a fast change DOP from 60% to 90%, indicating strong polarization instability. Therefore, such slow breathing behavior originates from the longitudinal and orthogonal polarization modes synchronization (constant phase difference) and desynchronization (phase difference slip). The polarimetric measurement also provides a route to identify desynchronization by visualizing the SOP evolution of the DS breathing. We then evidenced the desynchronization of polarization modes on the surface of the polarization Poincaré sphere [Fig. 2(e)], from which the SOP takes the form of hops from a localized point.

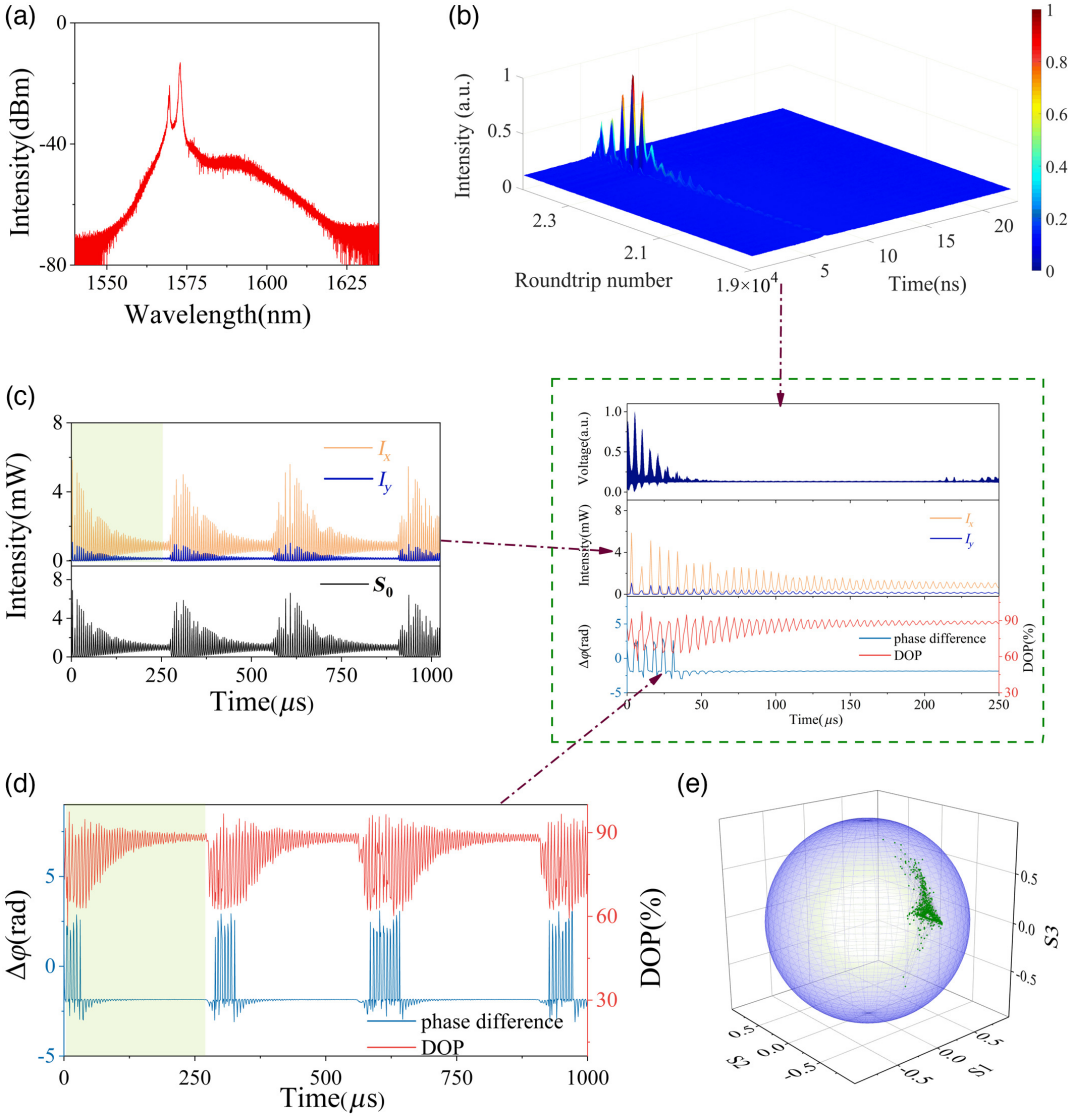

Fig. 2 Experimental observation of slow vector DS breathing dynamics. (a) Optical spectrum with dual-peak feature at 1570 nm; (b) single shot temporal trace of vector DS breather. The period of breather is 10,000 RTs. Inset: zoomed in temporal structure of vector DS breather with a width of ~200 RTs; (c) slow polarimetric trace of powers of the orthogonally polarized components I_x (blue) I_y (orange) at a scale of 1 ms. The lower figure is the total power $I = I_x + I_y$ (black). Inset: zoomed-in temporal trace of shaded area in (c) within 250 μs (10,000 RTs), and the pulse period is ~200 RTs. (d) Slow polarimetric measurement retrieved breather phase difference $\Delta\phi$ (blue) and DOP (red) within 1 ms. When breathing appears, DOP oscillates between 60% and 90%, and $\Delta\phi$ oscillates within π. Inset: zoomed-in phase difference transition and DOP of shaded area in (d) within 250 μs. (e) SOP evolution trajectories of vector DS breathing on the surface of Poincaré sphere within 1 ms. All stokes parameters are normalized. Note: The laser pump power is $I_p = 500$ mW.

The vector DS breathing waveform can survive hours under lab conditions. Further, increasing pump power would result in completely unstable mode locking. Nevertheless, the NPR mechanism offers control of the polarization dimension, thus providing access to various stable DS regimes such as DS molecules and noise-like pulses in our laser under fixed pump power (see Appendix B, Sec. 5.1). In a laser, the undamped relaxation oscillation mechanism of Q-switching intrinsically generates breathers at a longer time scale. By adjusting the PCs in our laser, we could obtain another breathing state that is typically named Q-switched mode locking (QML). To examine the vector feature of breathing, we again carried out optical spectral measurement, temporal trace record, and polarimetric measurement, as shown in Fig. 3. Figure 3(a) shows the typical optical spectrum of a breather with the signature dual-peak feature. The rectangular pedestal in the optical spectrum indicates spectral filtering induced strong dissipative effects within the normal dispersion MLL cavity. In Fig. 3(b), the double-scaled temporal pulses show Q-switching behavior with a kilohertz repetition rate, i.e., 200 kHz (~200 RTs). Uniquely, there

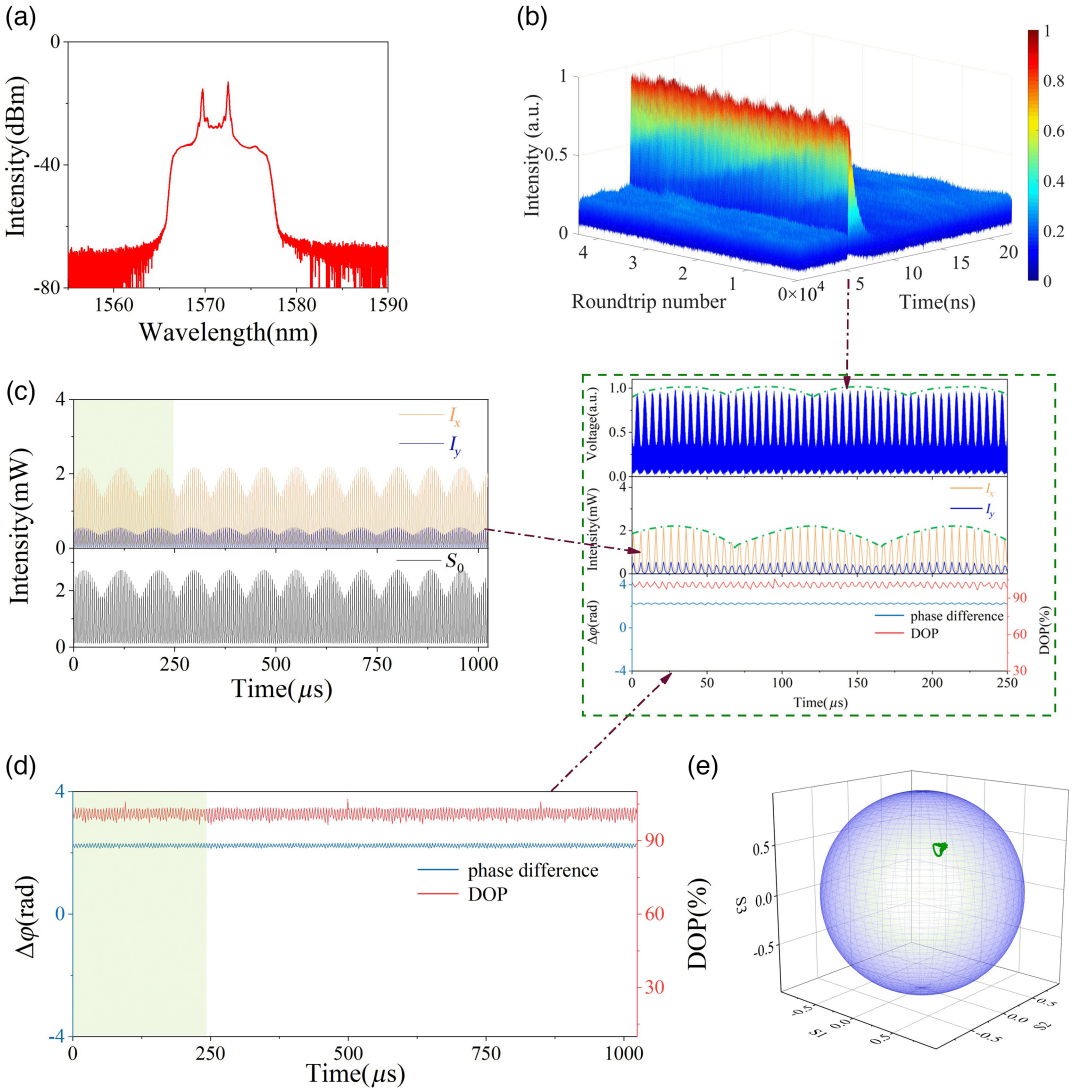

Fig. 3 Experimentally observed vectorial breathing dynamics of QML in a normal dispersion fiber laser. (a) Optical spectrum with a dual-peak feature for vector breathers. (b) Single-shot temporal trace of *Q*-switched mode-locked DS for 10,000 RTs. The period of the breather is 3000 RTs. Inset: zoomed-in temporal structure of the breather within 250 μs in shaded areas of (b). (c) Polarimeter measured averaged powers of the orthogonally polarized components I_x (blue) and I_y (orange). The lower figure is the total output power and total $S_0 = I_x + I_y$ (black). The period of the breathing waveform is ~4000 RTs. Inset: zoomed-in temporal trace within 250 μs in the shaded area of (c). (d) Retrieved phase difference $\Delta\varphi$ (blue) and DOP (red) through polarimetric measurement along 1 ms (44,000 RTs). Inset: zoomed-in phase difference evolution and DOP within 250 μs in the shaded area of (d). (e) SOP trajectories of *Q*-switched mode-locked breathers on polarization Poincaré sphere. All Stokes parameters are normalized. Note: The laser pump power is $I_p = 360$ mW.

appears another envelope of the *Q*-switching mode-locked pulses in addition to the general *Q*-switched pulse bunch. This slow envelope hence corresponds to the breathing QML pulses. The breathing period is 66 μs (3000 RTs). Through polarimetric measurement, the intensity discrepancy between orthogonal polarization modes can be well identified, indicating the vector feature of QML pulses [Fig. 3(c)]. A zoomed-in pulse oscillation is shown with a period of 200 RTs corresponding well to the fast detected results of this new type of slow vector breather. Moreover, by investigating the DOP of QML, we found that the DOP maintained ~100% at a large time window of 5000 RTs, as shown in Fig. 3(d). Such high DOP implies that the dynamic SOP is indeed slow and can be finely resolved through our polarimetric measurement. Moreover, the phase change in Fig. 3(d) appears as a straight line with finite thickness. This depicts an observable change without sudden slip in the phase domain [inset in Fig. 3(d)]. The dynamic temporal oscillation is therefore caused by the phase difference entrainment of orthogonal fields. The resulting Poincaré sphere representation of SOP trajectory [Fig. 3(e)] hence forms a limited cycle, indicating phase difference entrainment synchronization of the vector breathers.[15,28]

2.2 Vector Model of Er-Doped Mode-Locked Fiber Laser

For modeling slow breathing dynamics, we developed a vector model for a mode-locked EDF laser (details are in Appendix A, Sec. 4.2). This model overcomes limitations of the previous scalar or even vector models such as coupled nonlinear Schrödinger or Ginzburg–Landau equations, where long-range pulse dynamics are missing. Our model mainly visits the orientation distribution of the dipole moments with absorption and emission, the temporal response of the active medium's population inversion, linear, and circular birefringence of a laser cavity and pump light contribution. We adopt the slow evolution of the lasing field in terms of the Stokes vector $S = (S_0, S_1, S_2, S_3)^T$, and orientation distribution of the active medium's population inversion in terms of Fourier coefficients for angular distribution of the population inversion $f_i = (f_1, f_2, f_3)$, initial equations were averaged over the pulse width. For emulating the contribution of NPR, we take the linear β_L and circular β_C birefringence into consideration, where $\beta_{LC} = 2\pi L/L_{bL(bC)}$, $L_{bL(bC)}$ is the linear (circular) birefringence beat length and L is the cavity length. We also involve the pump light anisotropy ξ in addition to the normalized pump power I_p, hence reflecting a completely vectorial treatment of laser pulse [Eq. (4) in Appendix A, Sec. 4.2]. To investigate the phase synchronization scenarios in vector DS, we simply derive the equation for the phase difference between orthogonal polarization states using our vector model [Eq. (6) in Appendix A, Sec. 4.2]. The slow-varying phase difference relationship is similar to the Adler equation. Moreover, the presence of dynamically evolving Stokes parameters and orientation distribution of the population inversion in active medium manifests a new system in the MLL that is a coupled oscillator with dynamically evolving frequency difference and coupling.

We then map the breather's emergence in the phase space with the variables mentioned above. To identify the range parameters, i.e., the normalized pump power I_p, pump anisotropy ξ, and the linear birefringence β_L, we linearized Eq. (4) in Appendix A, Sec. 4.2 in the vicinity of the steady-state solution ($S_0 \neq 0,\ S_1 = S_2 = 0,\ S_3 = \pm S_0$) and found numerical eigenvalues for the parameters. Using the Shil'nikov theorem, eigenvalues λ and the second saddle parameter σ_2 take the form[41]

$$\lambda_0 = 0,\ \lambda_{1,2} = -\gamma_1 \pm i\omega_1,\ \lambda_{3,4} = -\gamma_2 \pm i\omega_2,$$
$$\lambda_{5,6} = \rho \pm i\omega_3,\ \sigma_2 = 2\cdot(\rho - \gamma_1).$$
$$(\omega_{1,2,3} \neq 0, \rho, \gamma_1, \gamma_2 > 0, \gamma_1 > \gamma_2). \tag{2}$$

Given that eigenvalues for steady states ($S_0 \neq 0,\ S_1 = S_2 = 0,\ S_3 = S_0$) and ($S_0 \neq 0,\ S_1 = S_2 = 0,\ S_3 = -S_0$) are equal, $\sigma_2 > 0$ hint condition for the orthogonal SOPs desynchronization.[28,30,32,33] The oscillatory behavior emerges when $\rho > 0$, indicating laser pulsation. Figure 4 shows the self-pulsing map under various laser operation conditions. Figures 4(a)–4(c) show the laser pulsing parameter regions for the anisotropic pump, birefringent cavity, and fixed pump power individually. The area covered by the colored contour surface locates the region of vector breathers' existence. At a fixed pump power, Fig. 4(d) identifies the conditions for Shil'nikov chaos.[41] According to the Shil'nikov theorem, condition $\sigma_2 > 0$ enables mapping the range of parameters where hyperchaotic behavior emerges.[41] The hyperchaotic trajectory is characterized by extreme sensitivity to the perturbations of the initial conditions or the system parameters. From Fig. 4, it is easy to observe that in the phase space, the oscillation exists in a quite wide range of pump power. However, the allowed range of pump anisotropy and intracavity birefringence strength for oscillation emergence is very limited, i.e., $0 < \xi < 0.5$, $0 < \beta_L < 0.006$. This explains why the slow breathing oscillations are difficult to observe

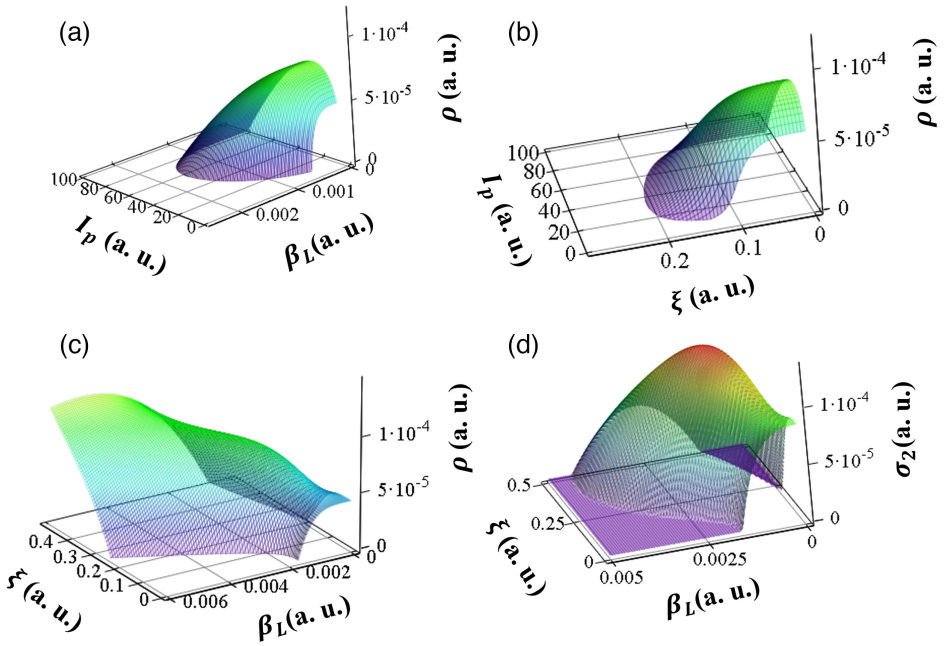

Fig. 4 Self-pulsing maps of laser operation conditions for $\rho > 0$, $\omega \neq 0$. (a) The pump wave is isotropic where $\xi = 0$. (b) The laser cavity is isotropic where $\beta_L = 0$. (c) The pump power is fixed. (d) Shil'nikov chaos conditions for the second saddle parameter σ_2 at $I_p = 55$.

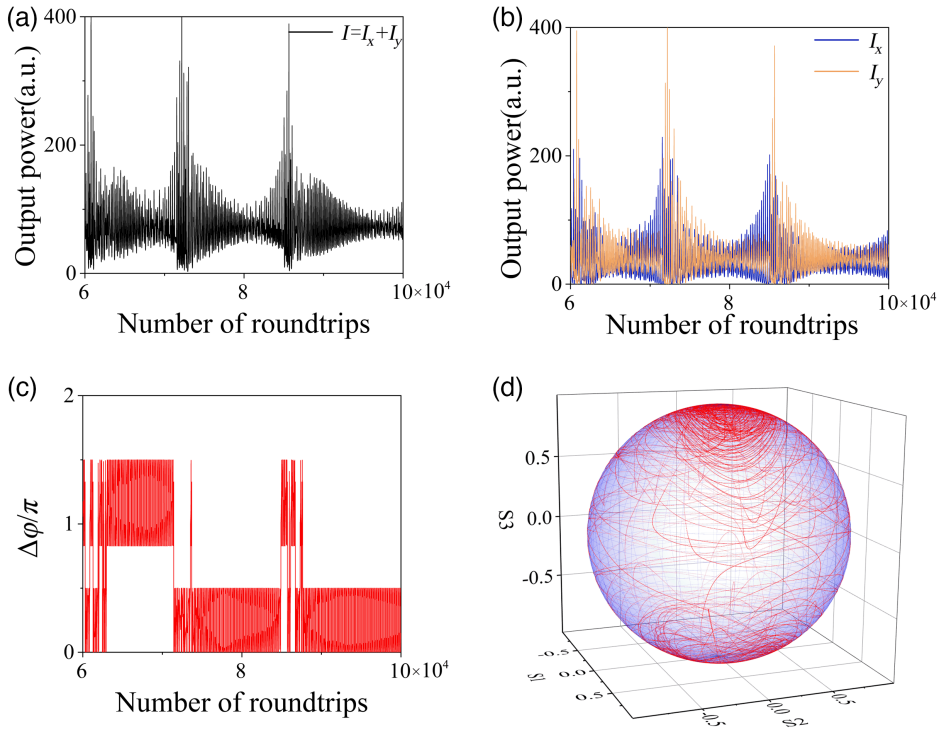

Fig. 5 Simulation of desynchronized vector breathing dynamics. (a) Breathing polarization dynamic in the form of complex oscillations of the total output power $I = I_x + I_y$. The breathing period is 104 RTs. (b) The simulated powers of the individual polarization components I_x (blue) and I_y (orange). (c) The calculated phase difference $\Delta\varphi$ between orthogonal polarization modes. The phase slip in π accords to the intensity breathing in (a). (d) SOP trajectories shown on the Poincaré sphere in normalized Stokes parameters. Note: Main parameters used in the model are $\beta_L = 2\pi \cdot 0.001$, $\beta_c = 0$, $I_p = 55$, $\sigma = 0.9$ ($\xi = 0.11$). The other parameters $\Delta = 0.025$, $\varepsilon = 0.22 \cdot 10^{-5}$, $\alpha_1 = 12.9$, $\alpha_2 = 2.3$, $\chi_s = 2.3$, $\chi_p = 1$, and $\gamma = 2 \cdot 10^{-6}$.

experimentally. Given that the dynamics in the model is averaged over the pulse width, the breathing dynamics of DS correspond to the phase difference desynchronization, the slow complex oscillations (Q-switched mode locking), and finally the steady-state operation (continuous-wave mode locking; see Appendix B, Fig. 7).

The simulated tunability of the breathing dynamics along with alternating the ellipticity of the pump wave is shown in Fig. 5. As shown in Fig. 5, the weak linear birefringence and low anisotropy of the pump wave within the range of parameters correspond to a case of $\sigma_2 > 0$ from which the laser operates under the breathing regime. The breather polarization dynamics reproduced in Figs. 5(a)–5(c) is quite close to the experimental observation shown in Figs. 2(c) and 2(d) in the context of shape, breathing period ($\sim$10,000 RTs) and the phase difference slips in π radian. The main deviation from the experimental observation is the Poincaré sphere SOP trajectories that can be caused by the simplified matter of the model that does not take into account the dual-wavelength lasing shown in Fig. 2(a) and slow polarimeter operation with a sampling of 50 RTs. Nevertheless, the SOP trajectories still follow a heteroclinic path.

As follows from Eq. (4) in Appendix A, Sec. 4.2, the increased pump anisotropy from $\xi = 0.11$ to $\xi = 0.22$ leads to a more anisotropic distribution of the population inversion (f_3 function) and so to enhanced coupling of the polarization components I_x and I_y. So, the chaotic behavior is transformed into periodic oscillations of the total's [Fig. 6(a)] and polarization components' powers [Fig. 6(b)], along with the periodic oscillations of the phase difference [Fig. 6(c)]. The simulated polarization dynamics is also quite similar to the experimental results shown in Figs. 3(c) and 3(d). The heteroclinic SOP trajectories further confirm the validity of our model. The main difference is that the trajectories on the Poincaré sphere can be caused by the dual-wavelength lasing shown in Fig. 3(a) and the low polarimeter sampling rate.

3 Discussion and Conclusion

We have experimentally demonstrated the observation of slow vector DS breathing waveforms in a normal dispersion mode-locked fiber laser. Such a dynamic pulse regime is obtained in the laser cavity well above the lasing threshold. We have shown numerically that such a type of breathing dynamics exists not only through the balance of gain, loss, dispersion, and nonlinearity, but also more to an equilibrium based on pump wave ellipticity, cavity anisotropy, and intracavity birefringence. The developed vector model reproduced our experimental observation well. We have identified the region for vector DS breathing emergence. The pump power and cavity birefringence can be controlled to alter the coupling strength between orthogonal SOPs. Uniquely, we have linked the appearance of vector DS breathing regime with the general synchronization

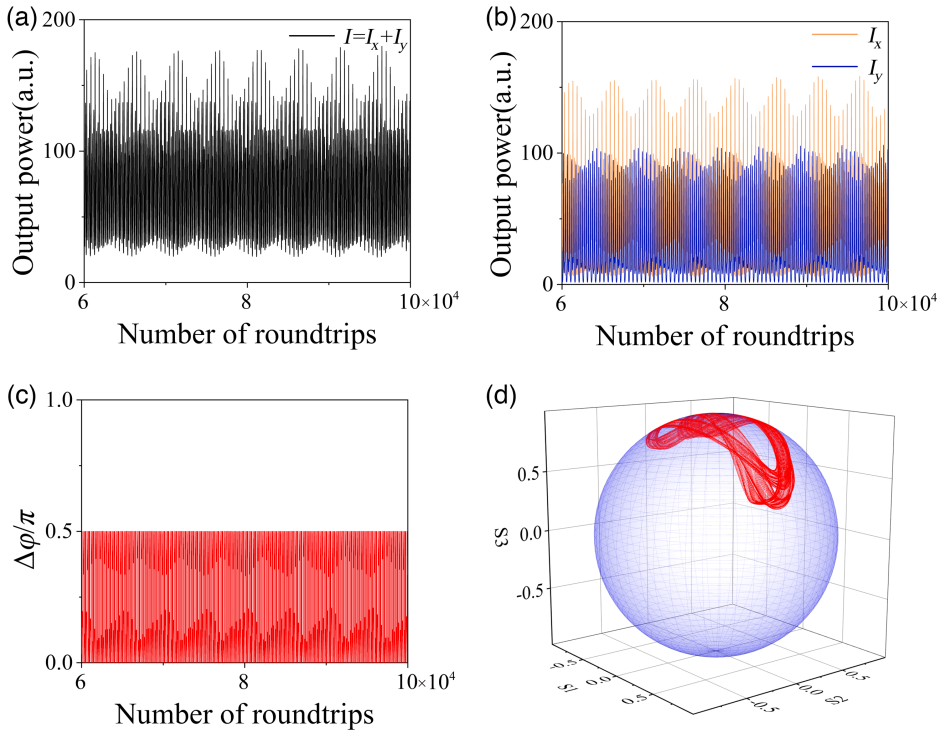

Fig. 6 Simulation of phase difference entrainment vector breathing dynamics. (a) Simulated temporal trance in the form of complex oscillations (QML) of the output power total power $I = I_x + I_y$. The breathing period is 3000 RTs. (b) Simulated temporal trace of the powers of polarization components I_x and I_y. The breathing period is 3000 RTs. (c) Simulated phase difference $\Delta\phi$ evolution along 10,000 RTs. (d) SOP trajectories in the Poincaré sphere. The main parameters used in the model are $\sigma = 0.8$ ($\xi = 0.22$), $\beta_L = 0$, $\beta_C = 2\pi \cdot 0.001$, $I_p = 55$. The other parameters: $\Delta = 0.025$, $\varepsilon = 0.22 \cdot 10^{-5}$, $\alpha_1 = 12.9$, $\alpha_2 = 2.3$, $\chi_s = 2.3$, $\chi_p = 1$, $\gamma = 2 \cdot 10^{-6}$.

concept in the phase domain through orthogonal polarization mode coupling. Weak coupling leads to the polarized modes' desynchronization, with periodic switching SOPs trajectories evolving around a fixed point, which corresponds well to the heteroclinic dynamics.[41] Compared with the existing soliton breathers, the vector breathing period (dwelling time near each SOP) in the scale of thousands of cavity RT times is approximately 2 orders of magnitude longer than that for scalar breathers. This is in stark contrast to the previous vector DS breathing waveforms (breathers and QS-mode locked) observed experimentally and theoretically.[34–36]

Our results demonstrate that the slow vector DS breathing universally exists in a normal dispersion mode-locked fiber laser. Our investigation can contribute to the thoroughgoing understanding of DS and laser physics. With the vector model, observations further illustrate that the mode-locked fiber laser serves as an effective test bed for the study of complex nonlinear dynamics relevant to a large variety of physical systems in a higher dimension. Likely, similar slow vector DS breathing waveforms may also exist in other types of MLLs. Further detailed breathing dynamics may be characterized through polarization-resolved dispersive Fourier transform in the future. Our findings could help in designing an ultrastable high-power mode-locked fiber laser, from which frequency comb, machining, and metrology would find important applications. It is also anticipated that the observed breathing dynamics is not only limited to nonlinear optics but also benefits in discovering new dynamics in general nonlinear physics, plasmonics, biology, and materials science.

4 Appendix A

4.1 Experimental Design

The configuration of the NPR mode-locked fiber laser is shown in Fig. 1. A 1.48 m EDF with a normal GVD of +66.1 ps^2/km is used in this cavity. In addition, the cavity also contains 0.9 m of OFS980 fiber with a normal GVD of +4.5 ps^2/km and 2.34 m of a single-mode fiber with an anomalous GVD of −21.67 ps^2/km. The total length of the cavity is 4.72 m, corresponding to the fundamental frequency of 44.18 MHz and the net dispersion of the cavity is +0.046 ps^2, and so the laser operates in the normal dispersion. The pump light is coupled to the laser cavity through a 980/1550 nm wavelength division multiplexer (WDM). A 91:9 coupler is used to direct out 9% of the pulse energy outside the cavity. The polarization-insensitive isolator (PI-ISO) in the cavity makes the unidirectional pulse train propagation. A fiber polarizer and two PCs are used to support the NPR mechanism for passive mode locking. By using the fast photodetector and oscilloscope, we record the dynamics of waveforms. By utilizing a commercial polarimeter (THORLABS, IPM5300) with 1 μs resolution, we observed the evolution of the polarization attractors at the Poincaré sphere in terms of the normalized Stoke parameters S_1, S_2, and S_3, the

power for the orthogonal x and y polarization components (I_x, I_y), the total power S_0, the phase difference $\Delta\varphi$, and the DOP. The definition of raw/normalized Stokes parameters and DOP is given below,

$$\begin{aligned}
&S_0 = I_x + I_y,\\
&S_1 = I_x - I_y,\\
&S_2 = 2\sqrt{I_x I_y}\,\cos\,\Delta\varphi,\\
&S_3 = 2\sqrt{I_x I_y}\,\sin\,\Delta\varphi,\\
&s_i = S_i/\sqrt{S_1^2+S_2^2+S_3^2},\\
&\mathrm{DOP} = \sqrt{S_1^2+S_2^2+S_3^2}/S_0,\ (i=1,2,3).
\end{aligned} \tag{3}$$

4.2 Vector Model of Erbium-Doped Fiber Laser

$$\begin{aligned}
\frac{dS_0}{dt} &= \left(\frac{2\alpha_1 f_1}{1+\Delta^2} - 2\alpha_2\right)S_0 + \frac{2\alpha_1 f_2}{1+\Delta^2}S_1 + \frac{2\alpha_1 f_3}{1+\Delta^2}S_2,\\
\frac{dS_1}{dt} &= \gamma S_2 S_3 + \frac{2\alpha_1 f_2}{1+\Delta^2}S_0 + \left(\frac{2\alpha_1 f_1}{1+\Delta^2} - 2\alpha_2\right)S_1\\
&\quad - \beta_c S_2 - \frac{2\alpha_1 f_3 \Delta}{1+\Delta^2}S_3,\\
\frac{dS_2}{dt} &= -\gamma S_1 S_3 + \frac{2\alpha_1 f_3}{1+\Delta^2}S_0 + \beta_c S_1 + \left(\frac{2\alpha_1 f_1}{1+\Delta^2} - 2\alpha_2\right)S_2\\
&\quad + \left(\frac{2\alpha_1 f_2 \Delta}{1+\Delta^2} - 2\beta_L\right)S_3,\\
\frac{dS_3}{dt} &= \frac{2\alpha_1 \Delta f_3}{1+\Delta^2}S_1 - \left(\frac{2\alpha_1 \Delta f_2}{1+\Delta^2} - 2\beta_L\right)S_2 + \left(\frac{2\alpha_1 f_1}{1+\Delta^2} - 2\alpha_2\right)S_3,\\
\frac{df_1}{dt} &= \varepsilon\left\{\frac{(\chi_s - 1)I_p}{2} - 1 - \left(1 + \frac{I_p\chi_p}{2} + d_1 S_0\right)f_1\right.\\
&\quad \left. - \left[d_1 S_1 + \frac{I_p\chi_p}{2}\frac{(1-\delta^2)}{(1+\delta^2)}\right]f_2 - d_1 S_2 f_3\right\},\\
\frac{df_2}{dt} &= \varepsilon\left\{\frac{(1-\delta^2)}{(1+\delta^2)}\frac{I_p(\chi_s - 1)}{4} - \left(\frac{I_p\chi_p}{2} + 1 + d_1 S_0\right)f_2\right.\\
&\quad \left. - \left[\frac{(1-\delta^2)}{(1+\delta^2)}\frac{I_p\chi_p}{2} + d_1 S_1\right]\frac{f_1}{2}\right\}\\
\frac{df_3}{dt} &= -\varepsilon\left[\frac{d_1 S_2 f_1}{2} + \left(\frac{I_p\chi_p}{2} + 1 + d_1 S_0\right)f_3\right].
\end{aligned} \tag{4}$$

Here, time and length are normalized to the RT and cavity length, respectively. Coefficient $\alpha_1 = \sigma_a \Gamma_L c_{\mathrm{Er}}$ is the EDF absorption at the lasing wavelength, α_2 represents the normalized losses, S_i $(i = 0, 1, 2, 3)$ are the Stokes parameters; S_0 and I_p are the output lasing and the pump power normalized to the corresponding saturation powers I_{ss} and I_{ps}, respectively. Here, $I_{ps} = \gamma_d A h\nu_p/(\sigma_a^{(p)}\Gamma_p)$, $I_{ss} = \gamma_d A h\nu_s/(\sigma_a^{(L)}\Gamma_L)$ (h is the Planck's constant, ν_p, ν_s are pump and lasing frequencies), $\chi = (\sigma_a^{(L)} + \sigma_e^{(L)})/\sigma_a^{(L)}$, $\sigma_{a(e)}^{(L)}$, $\sigma_a^{(p)}$ are absorption and emission cross sections at the lasing wavelength and absorption cross section at the pump wavelength, Γ_L and Γ_p are the confinement factors of the EDF fiber at the lasing and pump wavelengths, c_{Er} is the concentration of erbium ions, and A is the fiber core cross-section area. Coefficient γ is normalized to the cavity length and the saturation power; the Kerr constant, $\varepsilon = \tau_R/\tau_{\mathrm{Er}}$, is the ratio of the RT time τ_R to the lifetime of erbium ions at the first excited level τ_{Er}; Δ is the detuning of the lasing wavelength with respect to the maximum of the gain spectrum (normalized to the gain spectral width); $d_1 = \chi_s/(1+\Delta^2)$. To mimic the contribution of the two PCs and polarizer shown in Fig. 1, we account for the linear β_L, and the circular β_C birefringence $\beta_{L(C)} = 2\pi L/L_{bL(bC)}$ is the linear (circular) birefringence beat length and L is the cavity length and the pump anisotropy $\xi = (1-\delta^2)/(1+\delta^2)$, where δ is the ellipticity of the pump wave.[28–30]

Equation (4) has been derived under the approximation that the dipole moments of the absorption and emission transitions for erbium-doped silica are located in the plane that is orthogonal to the direction of the light propagation. This results in the angular distribution of the excited ions $n(\theta)$, which can be expanded into a Fourier series as follows:[28–30]

$$\begin{aligned}
&n(\theta) = \frac{n_0}{2} + \sum_{k=1}^{\infty} n_{1k}\,\cos(k\theta) + \sum_{k=1}^{\infty} n_{2k}\,\sin(k\theta),\\
&f_1 = \left(\chi\frac{n_0}{2} - 1\right) + \chi\frac{n_{12}}{2},\ f_2 = \left(\chi\frac{n_0}{2} - 1\right) - \chi\frac{n_{12}}{2},\\
&f_3 = \chi\frac{n_{22}}{2}.
\end{aligned} \tag{5}$$

To explore the concept of the phase-coupled oscillators, by using Eqs. (4) and (5), we derive the equation for the phase difference between two orthogonal SOPs as follows:

$$\begin{aligned}
\frac{d\Delta\varphi}{dt} &= -2\beta_L + \frac{2\alpha_1 f_2 \Delta}{1+\Delta^2} - \frac{\gamma}{12}S_1[1 - 2\cdot\ \cos(2\Delta\varphi)]\\
&\quad + \frac{f_3}{2}\left(-\frac{S_1}{S_3}\frac{\Delta}{1+\Delta^2} + \frac{S_0}{S_2}\right)\sin(2\Delta\varphi).
\end{aligned} \tag{6}$$

The simulation for stable DS and another example of breather is shown in Appendix A, Sec. 4.2.

As follows from Eqs. (6) and (1), increased birefringence strength β_L and nonlinearity coefficient γ lead to increased frequency of oscillations. The dependence of the coupling coefficient in Eq. (6) on the dynamically evolving Stokes parameters results in alteration of the synchronization and desynchronization shown in Fig. 5(c) and so in breathing dynamics in Figs. 5(a) and 5(b). Also, the linear stability analysis [Eq. (2) and Fig. 4] demonstrates that the breathing dynamics exists for very narrow range of values of the birefringence strength and the pump anisotropy ξ. For an example, increasing the pump anisotropy leads to modification of breathing dynamics toward oscillations shown in Fig. 6.

5 Appendix B

5.1 Additional Experimental Results

In the experiment, we can achieve different mode-locking states by increasing the pump power or adjusting the PCs individually at the same pump power. Figure 7 shows continuous wave (CW) mode-locking state of DSs at a pump power of 260 mW. When the pump power is increased from 260 to 450 mW, the DS pulse splits into an unstable multi-pulse state in Fig. 8. After that, under this pump power, only adjusting the PCs can obtain unstable NLP in Fig. 9, stable NLP in Fig. 10, and stable DS in Fig. 11. Figures 12 and 13 show two different types of breathing waveforms from those in the article.

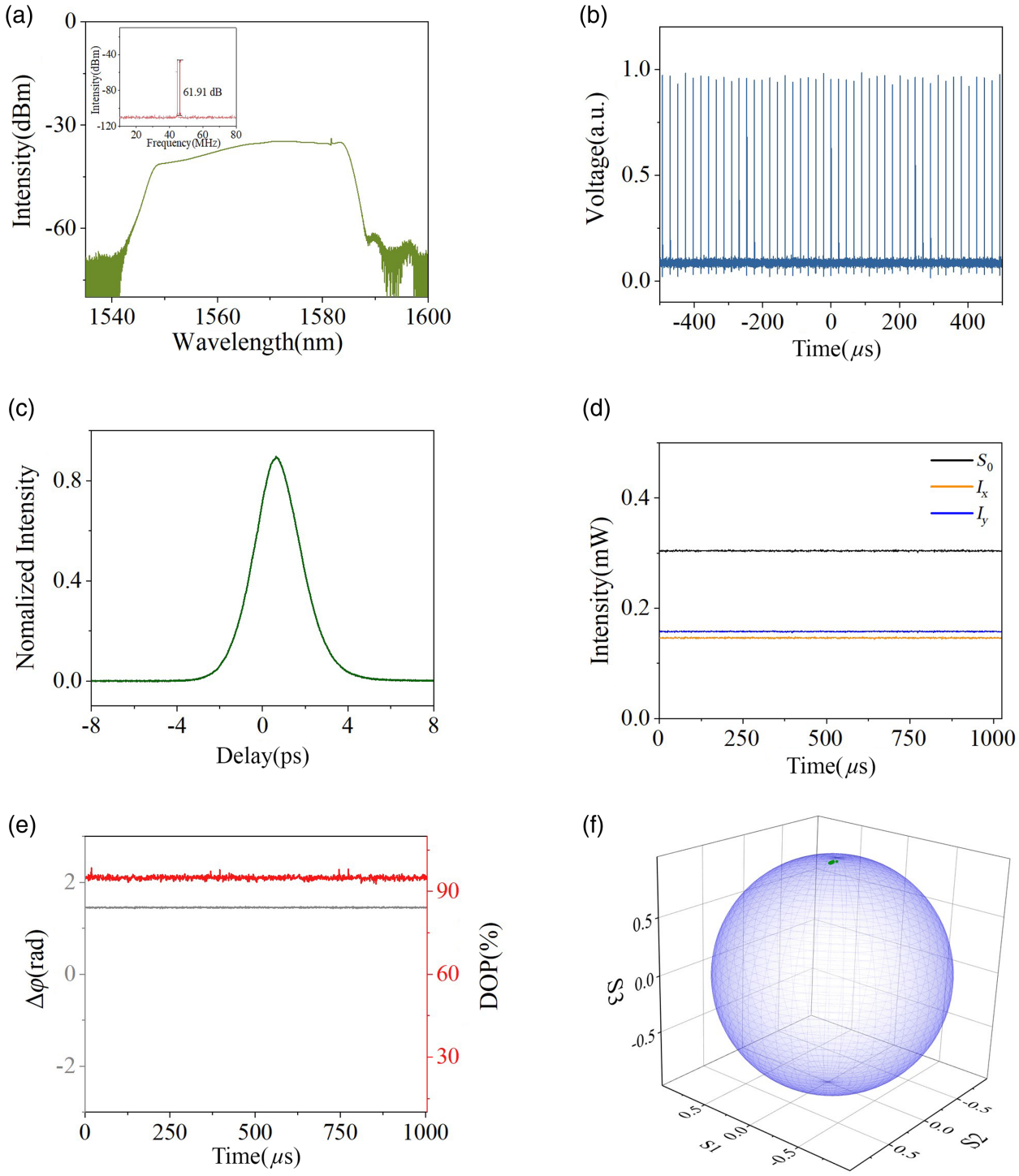

Fig. 7 CW mode-locking state of DSs with a locked state of polarization (SOP) at a pump power of 260 mW. The CW mode-locking case at a pump power of 260 mW of DS is shown in (a)–(e). The wide optical spectrum typical for the normal dispersion operation is shown in (a). (b) A stable mode-locking pulse train with a repetition rate of 44.18 MHz accords well with the length of the cavity, and the pulse train has a stable amplitude with the small variation of the peak power at the fast and slow time scales. (c) The autocorrelation trajectory. (d) The output power of two orthogonal polarization components giving stable evolving power. (e) The fixed phase difference and SOP locking with high DOP above 90%, indicating the soliton is polarization locked vector dissipative soliton (PLVDS) caused by strong coupling between two orthogonal polarization components. (f) The averaged SOP on the Poincaré sphere within 1 ms in the form of a fixed point.

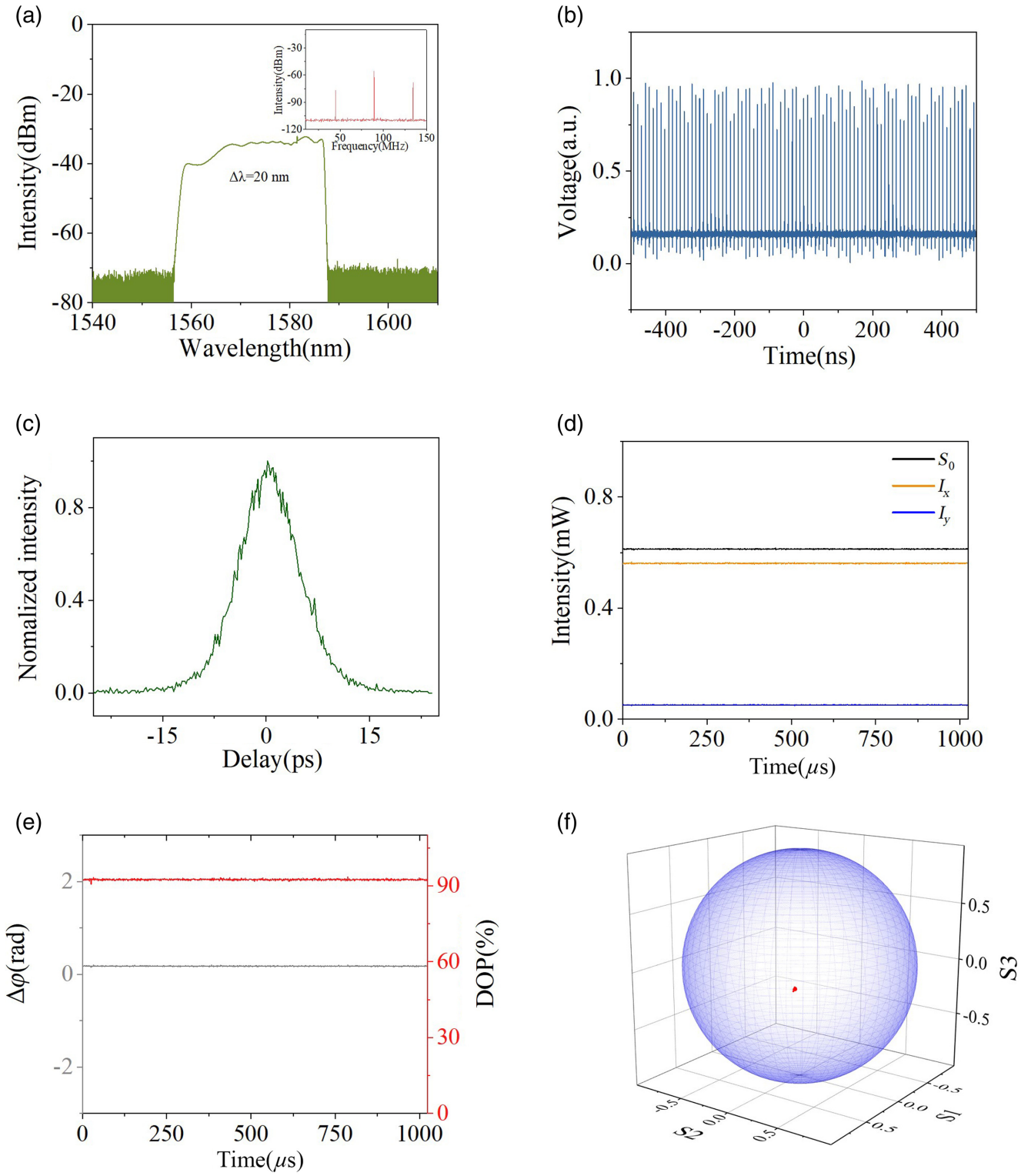

Fig. 8 Unstable multi-pulse states of DSs when the pump power is increased from 260 to 450 mW. When the pump power is increased from 260 to 450 mW, the stable fundamental frequency DSs become unstable multi-pulse states of DSs shown in (a). The pulse train has an unstable amplitude with a repetition rate of 88.36 MHz and pulse duration of ~10 ps, as shown in (b) and (c). (d), (e) The polarization state of the pulse, indicating the soliton is PLVDS so we cab increase the pump power to obtain an unstable mode-locking state. (f) The averaged SOP on the Poincare sphere within 1 ms in the form of a fixed point.

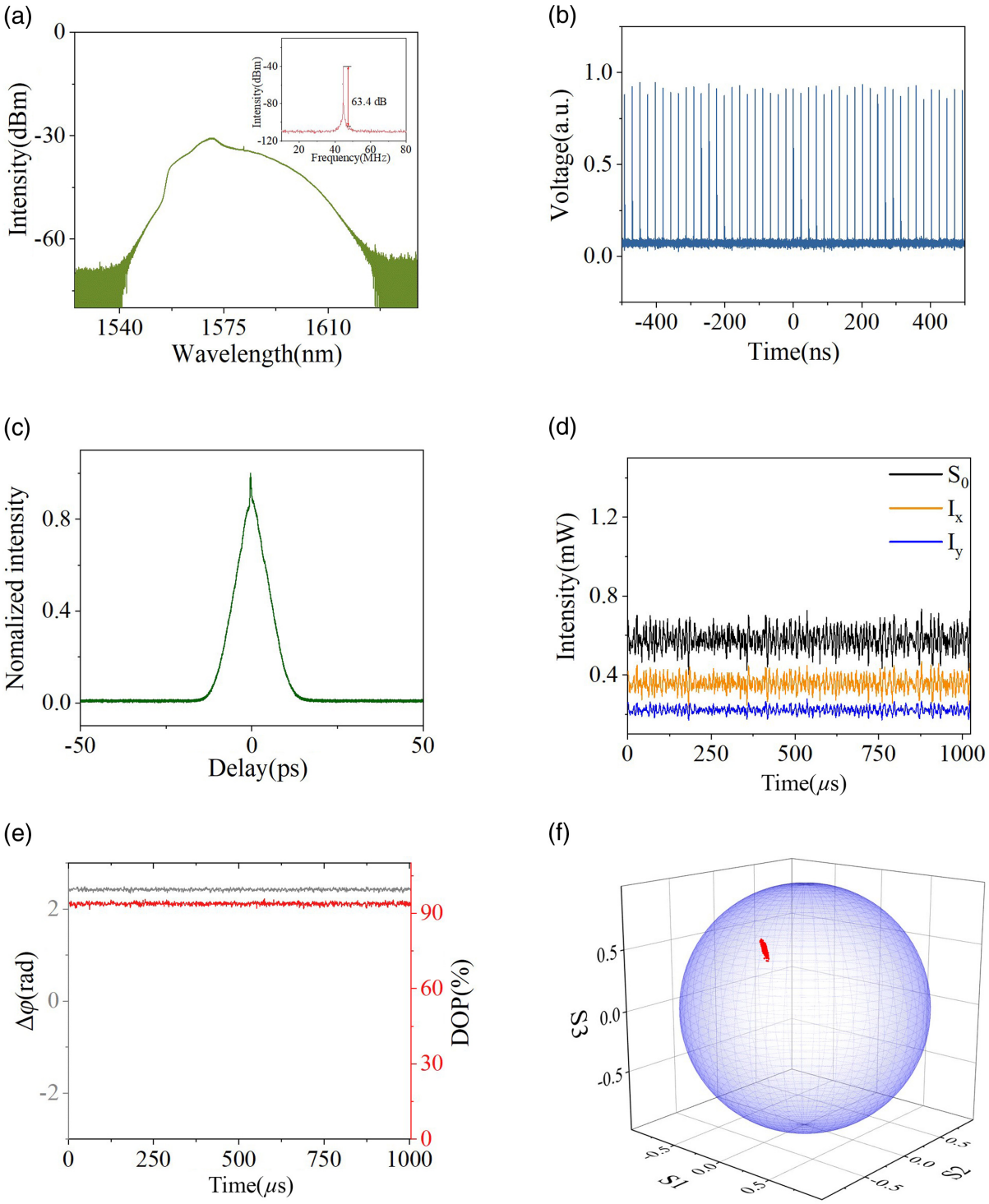

Fig. 9 Unstable mode-locking state of NLP at the same pump power as in Fig. 8. At the same pump power as Fig. 8, we can obtain NLP with polarization instability mode-locking state only by adjusting the PCs. (a) A typical spectrum of NLP. (b) The pulse with a repetition rate of 44.18 MHz accords well with the length of the cavity. (c) The autocorrelation trajectory, which is very consistent with the typical characteristics of NLP with a large energy base and a very narrow peak. As shown in (d) and (f), the output power of the cavity varies within a certain range, and the averaged SOP on the Poincaré sphere is not a fixed point, which indicates that the laser is not operating in a stable state, mainly due to the weak coupling of the strengths I_x and I_y. (e) The fixed phase difference and SOP locking with high DOP above 90%.

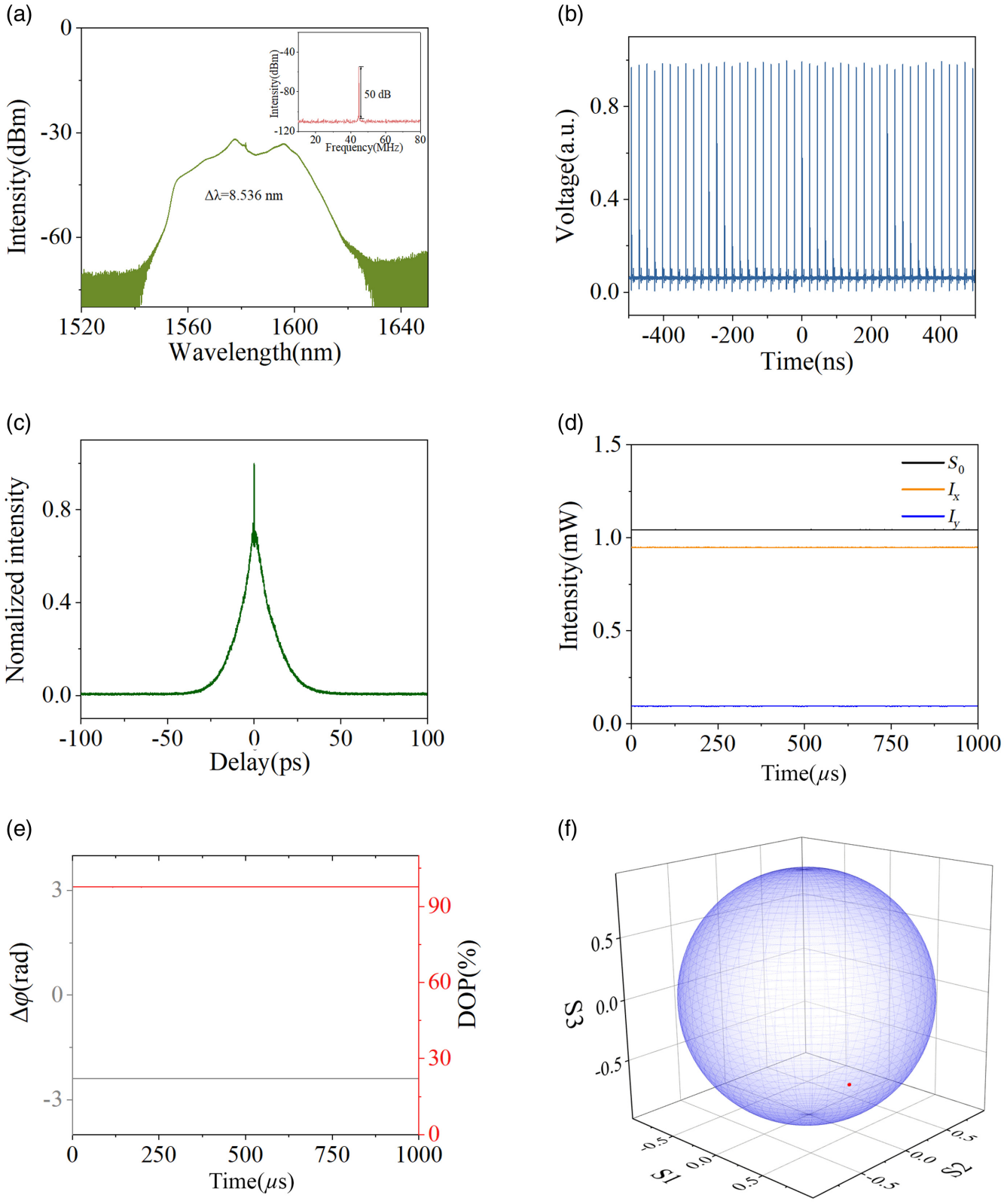

Fig. 10 (a) A typical spectrum of NLP. (b)A stable mode-locking pulse train with a repetition rate of 44.18 MHz accords well to the length of cavity and the pulse train has a stable amplitude. (c) The autocorrelation trajectory which is very consistent with the typical characteristics of NLP with a large energy base and a very narrow peak. As shown in (d) and (e), the output powers of two orthogonal polarization components keep unchanged with fixed phase difference and high DOP above 90% indicating that the soliton is polarization locked vector soliton (PLVS). (f) The averaged SOP on the Poincaré sphere within 1 ms in the form of a fixed point.

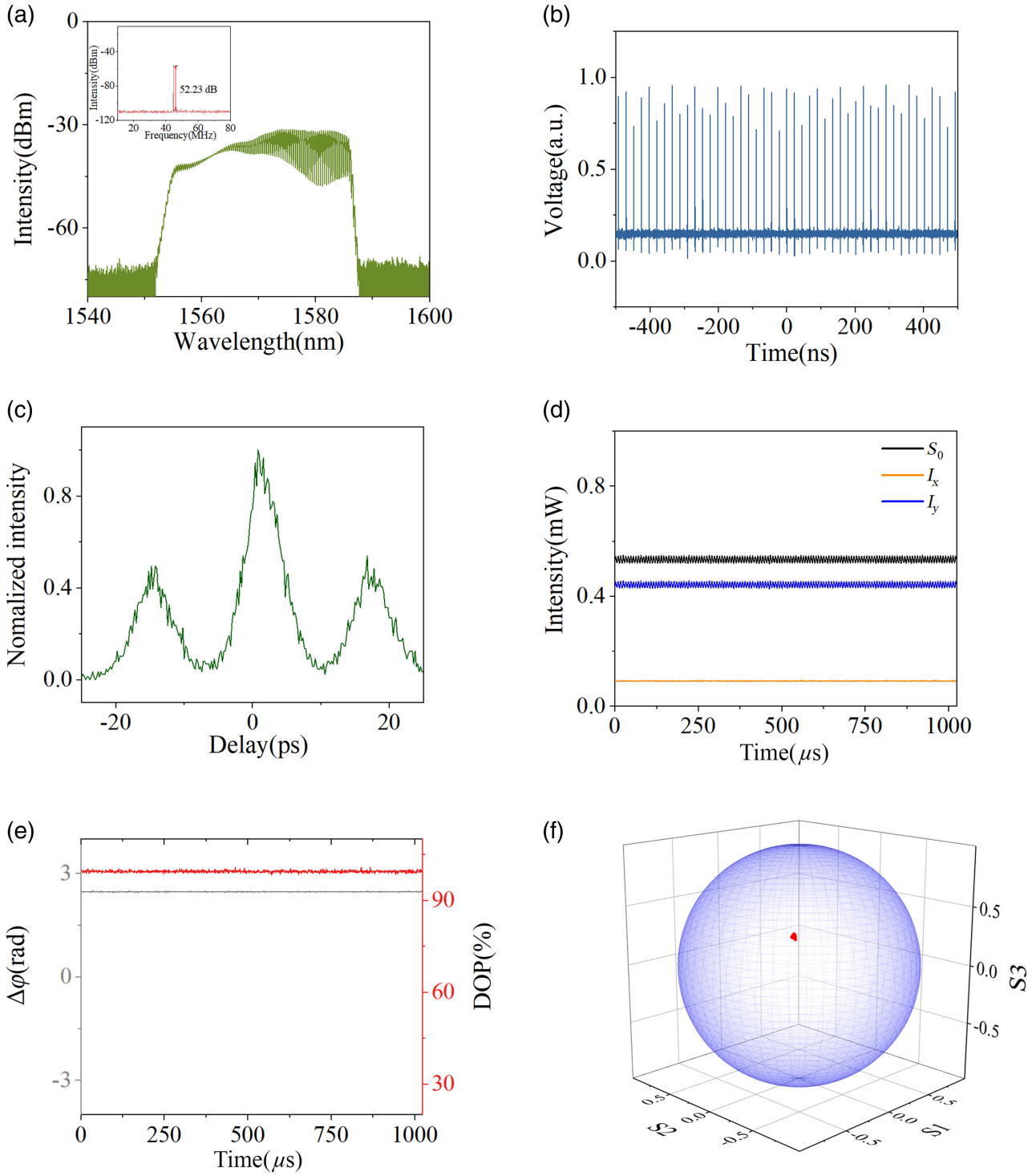

Fig. 11 Stable mode-locking state of DS molecules at the same pump power as in Fig. 9. At the same pump power as in Fig. 9, the CW mode-locking state of NLP can be turned into a stable mode-locking state of DS molecules with a locked SOP only by adjusting the PCs. (a) Significant regular periodic modulation, and the overall shape of the modulation spectrum has the typical characteristics of a single-pulse DS spectrum. As shown in (b), the bound state solitons as a whole propagate in the laser cavity with a repetition rate of 44.18 MHz. (c) An autocorrelation trajectory with three peaks. (d) The output power of two orthogonal polarization components varying within a certain range. (e) and (f) The fixed phase difference, a fixed point on the Poincaré sphere, and high DOP above 90%, which indicates that the soliton is PLVDS.

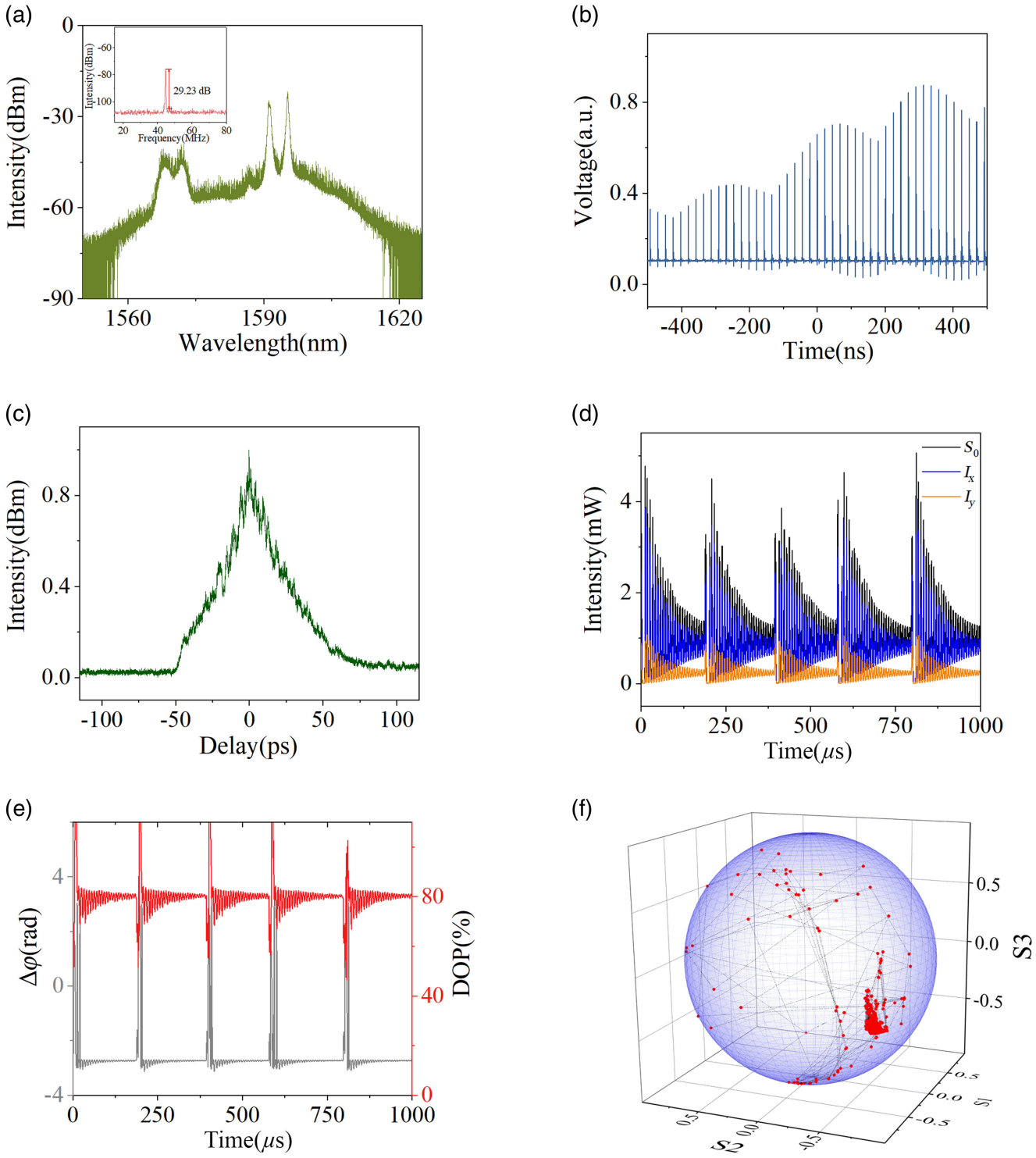

Fig. 12 Experimental observation of desynchronized vector breather dynamics. In addition to the breathers in the article, it can also be obtained desynchronized vector breather at the pump power of 500 mW. The optical spectrum, pulse trains, and autocorrelation trajectory are shown in (a)–(c), respectively. As shown in (a), the optical spectrum has two maxima that reflects the breathing spectral dynamics. (d) A breather width of 200 μs. (e) The breather's power spikes emergence and disappearance is related to the periodic phase difference slip in π and DOP hops. As shown in (f), the trajectories in the Poincaré sphere also take the form of hops from the localized SOPs.

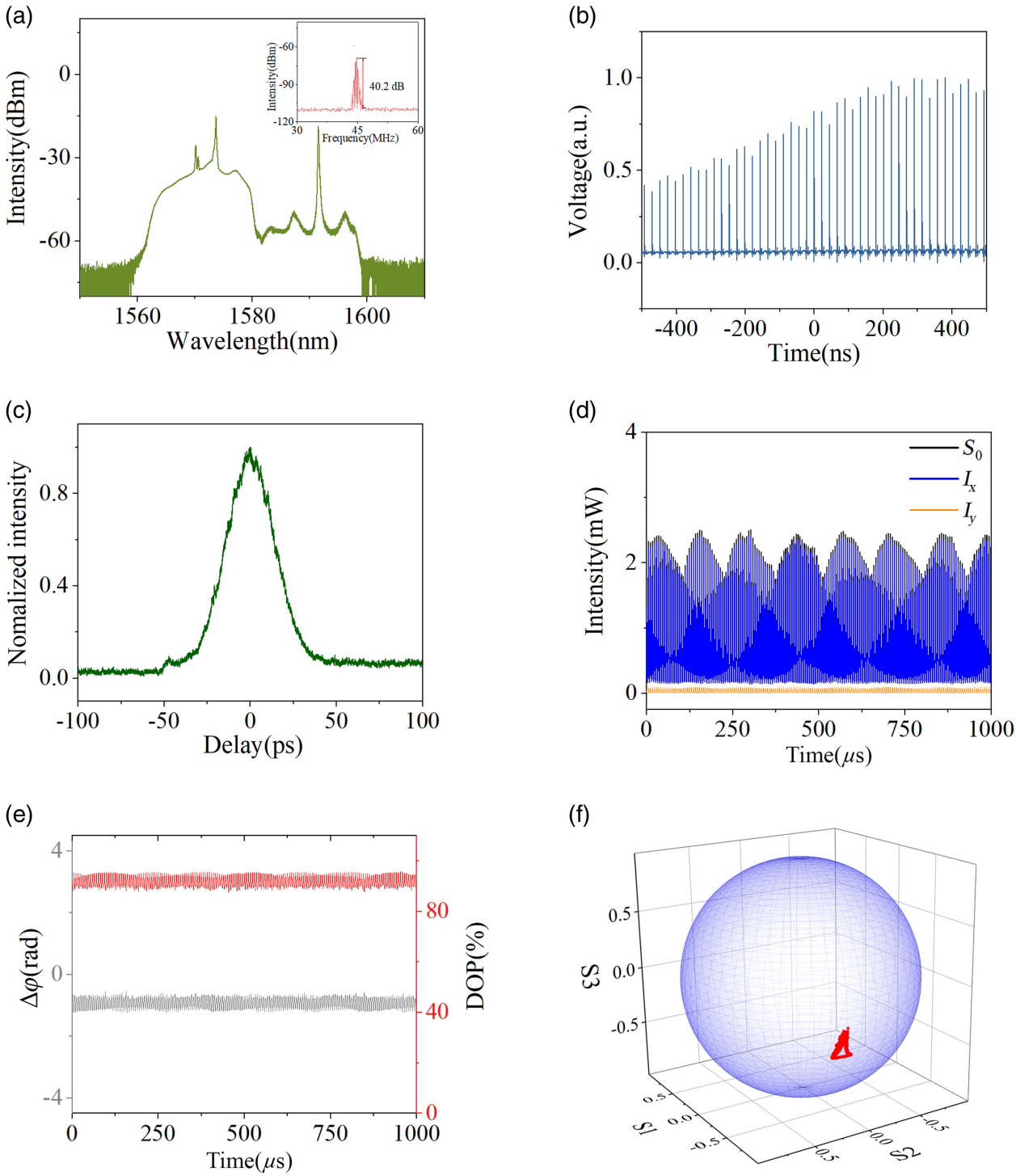

Fig. 13 Experimental observation of phase difference entrainment vector breather dynamics. In addition to the breathers in the article, a phase difference entrainment vector breather at the pump power of 460 mW can also be obtained. The optical spectrum, pulse trains, and autocorrelation trajectory are shown in (a)–(c), respectively. Similar to the previous case shown in Fig. 13, the optical spectrum in (a) also exhibits two maxima. However, the breathing dynamics takes the form of two-scale oscillations (QML) with the periods of 125 μs in (e). As follows from (d), the dynamics is caused by the phase difference entrainment (oscillations). The DOP above 90% indicates that the dynamic is slow at the time scale from 1 μs to 1 ms. As shown in (f), the trajectory in the Poincaré sphere is a cycle, and so the vector soliton breathing dynamics takes the form of a phase difference entrainment synchronization scenario.

5.2 Additional Theoretical Results

In addition to the simulation of vector breathing dynamics mentioned above, the breathing dynamics can also emerge for different circular birefringence and anisotropy of the pump wave as shown in Fig. 14. Figure 15 shows the simulation of polarization-locked regime which corresponds to the experimentally observed case shown in Figs. 7 and 10.

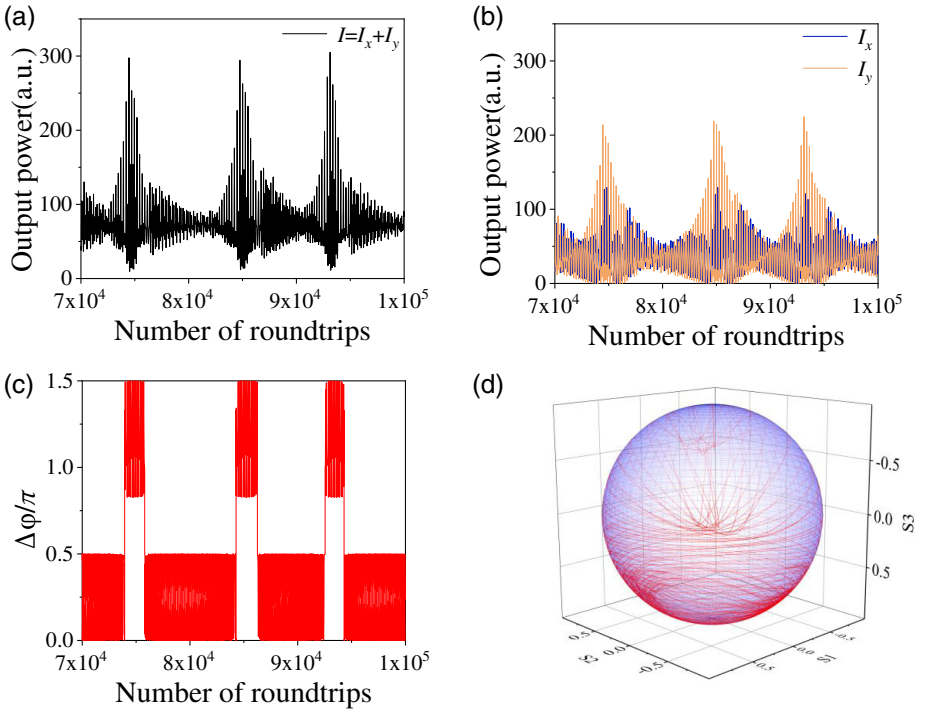

Fig. 14 Breathing polarization dynamics in the form of complex oscillations of the output power total power $I = I_x + I_y$. Though breathing regimes are not mapped in terms of the circular birefringence, the dynamics can also emerge for the weak circular birefringence and low anisotropy of the pump wave, as shown in (a)–(d). The main parameters: $\sigma = 0.95$ ($\xi = 0.05$), $\beta_L = 0$, $\beta_c = 2\pi \cdot 0.001$, $I_p = 55$. The other parameters: $\Delta = 0.025$, $\varepsilon = 0.22 \cdot 10^{-5}$, $\alpha_1 = 12.9$, $\alpha_2 = 2.3$, $\chi_s = 2.3$, $\chi_p = 1$, $\gamma = 2 \cdot 10^{-6}$. (a) and (b) The powers of the polarization components and the total power. As shown in (c), the phase difference slips in π radian. (d) SOP trajectories in the Poincaré sphere.

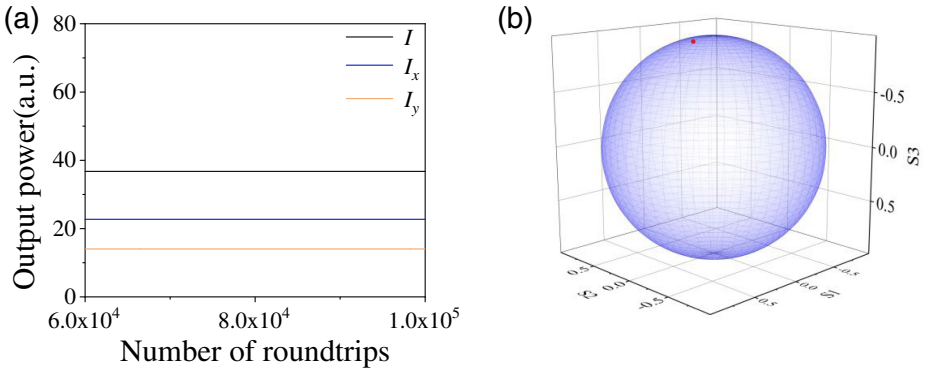

Fig. 15 Steady state (polarization-locked regime) in the form of the constant output powers. When the pump power is reduced from $I_p = 55$ to $I_p = 29$ and high pump anisotropy $\xi = 0.2$, it leads to the increase coupling between x and y components and so to the steady-state operation (CW or polarization-locked regime) shown in (a) and (b). The other parameters: $\Delta = 0.025$, $\varepsilon = 0.22 \cdot 10^{-5}$, $\alpha_1 = 12.9$, $\alpha_2 = 2.3$, $\chi_s = 2.3$, $\chi_p = 1$, and $\gamma = 2 \cdot 10^{-6}$.

Code and Data Availability

All data in support of the findings in this paper are available within the article or as supplementary materials.

Acknowledgments

The authors acknowledge the following funding support: The National Natural Science Foundation of China (Grant Nos. 61975107, 62075071, and 61605107), the '111' Project (Grant No. D20031), UK EPSRC (Grant No. EP/W002868/1), Leverhulme Trust (Grant No. HARVEST RPG-2023-073), and Horizon 2020 ETN MEFISTA (Grant No. 861152). The authors declare no conflicts of interest.

References

1. K. P. O'Keeffe, H. Hong, and S. H. Strogatz, "Oscillators that sync and swarm," *Nat. Commun.* **8**, 1504 (2017).
2. H. Mancini and G. Vidal, "Dynamics of two coupled chaotic systems driven by external signals," *Eur. Phys. J. D* **62**, 57 (2011).
3. W. Bialek et al., "Statistical mechanics for natural flocks of birds," *Proc. Natl. Acad. Sci. U. S. A.* **109**, 4786 (2012).
4. L. Minati et al., "Distributed sensing via inductively coupled single-transistor chaotic oscillators: a new approach and its experimental proof-of-concept," *IEEE Access* **7**, 174793 (2019).
5. Z. Chang et al., "Real-time dynamics of optical controlling for bound states of mode-locked fiber laser with short-range interaction," *Opt. Laser Technol.* **149**, 107859 (2022).
6. X. Wu et al., "Farey tree and devil's staircase of frequency-locked breathers in ultrafast lasers," *Nat. Commun.* **13**, 5784 (2022).
7. T. Xian et al., "Subharmonic entrainment breather solitons in ultrafast lasers," *Phys. Rev. Lett.* **125**, 163901 (2020).
8. Y. Du, Z. Xu, and X. Shu, "Spatio-spectral dynamics of the pulsating dissipative solitons in a normal-dispersion fiber laser," *Opt. Lett.* **43**, 3602 (2018).
9. J. Peng et al., "Breathing dissipative solitons in mode-locked fiber lasers," *Sci. Adv.* **5**, eaax1110 (2019).
10. J. M. Dudley et al., "Instabilities, breathers and rogue waves in optics," *Nat. Photonics* **8**, 755 (2014).
11. S. Chouli and P. Grelu, "Rains of solitons in a fiber laser," *Opt. Express* **17**, 11776 (2009).
12. S. Chouli and P. Grelu, "Soliton rains in a fiber laser: an experimental study," *Phys. Rev. A* **81**, 063829 (2010).
13. S. V. Sergeyev, M. Eliwa, and H. Kbashi, "Polarization attractors driven by vector soliton rain," *Opt. Express* **30**, 35663 (2022).
14. H. J. Kbashi et al., "Mulitiscale spatiotemporal structures in mode-locked fiber lasers," *Laser Phys. Lett.* **17**, 035103 (2020).
15. H. Kbashi et al., "Bright-dark rogue waves," *Ann. Phys., Lpz.* **530**, 1700362 (2018).
16. H. J. Kbashi et al., "Vector soliton breathing dynamics," *Laser Phys. Lett.* **16**, 035103 (2019).
17. X. Liu and M. Pang, "Revealing the buildup dynamics of harmonic mode-locking states in ultrafast lasers," *Laser Photonics Rev.* **13**, 1800333 (2019).
18. S. Sergeyev, S. Kolpakov, and Y. Loika, "Vector harmonic mode-locking by acoustic resonance," *Photonics Res.* **9**, 1432 (2021).
19. K. Sulimany et al., "Bidirectional soliton rain dynamics induced by Casimir-like interactions in a graphene mode-locked fiber laser," *Phys. Rev. Lett.* **121**, 133902 (2018).
20. W. He et al., "Formation of optical supramolecular structures in a fibre laser by tailoring long-range soliton interactions," *Nat. Commun.* **10**, 5756 (2019).
21. F. Sanchez et al., "Manipulating dissipative soliton ensembles in passively mode-locked fiber lasers," *Opt. Fiber Technol.* **20**, 562 (2014).
22. H.-G. Purwins, H. U. Bödeker, and S. Amiranashvili, "Dissipative solitons," *Adv. Phys.* **59**, 485 (2010).
23. N. Akhmediev and A. Ankiewicz, eds., *Dissipative Solitons*, Springer, Berlin, Heidelberg (2005).
24. M. Pang et al., "Stable subpicosecond soliton fiber laser passively mode-locked by gigahertz acoustic resonance in photonic crystal fiber core," *Optica* **2**, 339 (2015).
25. R. Weill et al., "Noise-mediated Casimir-like pulse interaction mechanism in lasers: supplementary material," *Optica* **3**, 189 (2016).
26. Y. Li et al., "Statistical dynamics of noise-like rectangle pulse fiber laser," *Adv. Photonics Nexus* **2**, 036005 (2023).
27. Y. Song et al., "Recent progress on optical rogue waves in fiber lasers: status, challenges, and perspectives," *Adv. Photonics* **2**, 024001 (2020).
28. S. Sergeyev and C. Mou, eds., *Polarization Dynamics of Mode-Locked Fiber Lasers: Science, Technology and Applications*, CRC Press Book Publishing (2023).
29. S. V. Sergeyev, "Fast and slowly evolving vector solitons in mode-locked fibre lasers," *Phil. Trans. R. Soc. A.* **372**, 20140006 (2014).
30. S. V. Sergeyev et al., "Spiral attractor created by vector solitons," *Light Sci. Appl.* **3**, e131 (2014).
31. Y. Du et al., "Alternation of the mode synchronization and desynchronization in ultrafast fiber laser," *Laser Photonics Rev.* **14**, 1900219 (2020).
32. C. Bao et al., "Observation of Fermi-Pasta-Ulam recurrence induced by breather solitons in an optical microresonator," *Phys. Rev. Lett.* **117**, 163901 (2016).
33. A. Mussot et al., "Fibre multi-wave mixing combs reveal the broken symmetry of Fermi-Pasta-Ulam recurrence," *Nat. Photonics* **12**, 303 (2018).
34. Y. Han et al., "Paths from stationary to chaos in passively mode-locked fiber lasers: research progress of soliton pulsations and soliton explosions," *J. Phys. B: At. Mol. Opt. Phys.* **55**, 222001 (2022).
35. Q. Wu et al., "Single-shot measurement of wavelength-resolved state of polarization dynamics in ultrafast lasers using dispersed division-of-amplitude," *Photonics Res.* **11**, 35 (2023).
36. Q. Wang et al., "Q-switched and vector soliton pulses from an Er-doped fiber laser with high stability based on a γ-graphyne saturable absorber," *Nanoscale* **15**, 7566 (2023).
37. C. P. Silva, "Shil'nikov's theorem: a tutorial," *EEE Trans. Circuits Syst. I Regul. Pap.* **40**, 675 (1993).
38. G. Ansmann et al., "Extreme events in excitable systems and mechanisms of their generation," *Phys. Rev. E* **88**, 052911 (2013).
39. A. Arenas et al., "Synchronization in complex networks," *Phys. Rep.* **469**, 93 (2008).
40. G. Tigan and D. Opriş, "Analysis of a 3D chaotic system," *Chaos, Solitons Fractals* **36**, 1315 (2008).
41. I. M. Ovsyannikov and L. P. Shil'nikov, "Systems with a homoclinic curve of multidimensional saddle-focus, and spiral chaos," *Math. USSR Sb.* **73**, 415 (1992).
42. A. Pikovsky, M. Rosenblum, and J. Kurths, *Synchronization: A Universal Concept in Nonlinear Sciences*, Cambridge University Press (2001).

Biographies of the authors are not available.